Characterising the effect of turbine operating point on momentum extraction of tidal turbine arrays

Christoph Hachmann*†, Tim Stallard*‡, Binliang Lin#††, Peter Stansby*§

*School of Mechanical, Civil and Aerospace Engineering
The University of Manchester, Oxford Road, M13 9PL, Manchester, United Kingdom
†christoph.hachmann@manchester.ac.uk
‡tim.stallard@manchester.ac.uk
§p.k.stansby@manchester.ac.uk

#State Key Laboratory of Hydro-science and Engineering
Tsinghua University, Beijing 100084, China
††linbl@mail.tsinghua.edu.cn

***Abstract*—Due to the predictable nature of the tides, power generation from tidal streams could play a significant role in addressing future power network challenges by providing an auxiliary frequency balancing service. A requirement of such services is that power output may be rapidly adapted. This can be achieved by several alternative operating strategies applied to individual turbines, to entire farms or to clusters of turbines within a farm. The onset tidal flow speed to an array is sensitive to the net resistance provided by the array and so it is necessary to consider how such strategies would affect power output, net resistance and the flow onset to the farm. Investigations using a Reynolds-averaged Navier-Stokes Actuator Disc (RANS-AD) model and experiments in a shallow channel are conducted to assess the influence of rotor operating point on individual turbine loading and hence aggregate resistance of an array. Array- and row-specific values for the local thrust coefficient and corresponding disc porosities are chosen to represent three typical operating values of turbine thrust and power.**

Both studies are assessed separately for turbine array configurations with up to 12 turbines deployed over 3 rows and in bi-directional flow. The results show good agreement with previous experimental and numerical publications. Additionally, similar trends are observed for the variation of the net array thrust coefficient with array layout and operating point for both studies. Application of these array operating points within a simple channel model indicates that the imposed net thrust can be reduced by 12.3% whilst the energy yield reduction over a 12 hour period is almost negligible. Thus, an adaptive operating strategy does not only provide more accurate information of the power output from tidal farms and reduces the environmental footprint of the latter, but also promotes a more flexible array operation which can facilitate a better grid integration of future large-scale tidal stream turbine arrays.

***Index Terms*—Tidal stream energy, Turbine arrays, CFD, Experiments, Operating points**

I. Introduction

Tidal stream energy systems are receiving increasing interest as a predictable renewable energy source (RES). Such systems could play a significant part in reducing greenhouse gas emissions and enabling a low-carbon society. Pilot projects are ongoing in multiple countries around the world to explore the potential of tidal stream energy. The technically exploitable resource available in UK waters alone is estimated to be around 20 TWh/year [1], around 7% of the domestic annual electricity consumption [2]. In April 2018, Phase 1A of the largest existing tidal stream turbine array MeyGen located in the Pentland Firth formally entered the operations phase with a duration of 25 years [3]. However, due to both the levels of electricity consumption and the limitations in terms of suitable tidal stream locations, farms with a much larger array capacity than MeyGen's current 6 MW are required to provide a meaningful contribution to the future energy mix.

One of the main advantages of tidal stream energy is the resource predictability. Hence, the power output can be deliberately manipulated to follow current electricity demand and provide ancillary frequency balancing services. The importance of such services as well as predictable energy sources is likely to increase in a future low-carbon energy market. A higher penetration of system frequency-decoupled RES such as wind and solar results in a reduced share of conventional synchronous power plants and in turn a decrease of the system inertia. Thus, the power network becomes more vulnerable towards sudden frequency changes and operational flexibility of generating power units more significant. As such, current operational standards in the UK include the ability to change the power output by 10% [4], [5].

Many studies of power generation from tidal stream systems have been conducted, including to quantify the maximum power output over a pre-defined time span [6]–[8] and to optimise turbine positions within arrays to maximise power output [9]–[11]. However, less attention has been given to prediction of the time-variation of power supply to inform network integration and assess the potential for tidal systems to contribute to system balancing. This includes the implementa-

tion of array- and row-specific turbine operating points within entire arrays to assess both the variation of power output as well as change of array drag and hence impact on the resource. Previous analysis by the authors [12] of a turbine array within an idealised channel model showed that different rotor operating points per row reduce the number of significant changes of hourly power output (ΔP >25% of the rated power, P_{rated}) by 40% whilst decreasing the power output by only 13%. This paper presents an investigation of the impact of such a changing operating point across a tidal farm on small multi-row turbine arrays, starting by characterising operating points of tidal turbines and presenting a potential computational modelling approach of the latter. An array-scale model is developed which consists of up to 12 tidal turbines and allows the implementation of turbine-specific operating points. This model is used to characterise the effect of varying operating points across entire rows and arrays and subsequently applied in an idealised channel-scale flow model to showcase the impact of the latter on both net array power output and thrust over a 12 hour tidal cycle. Finally, ongoing work is presented which includes aims to compare the numerical model with a recently undertaken experimental study.

II. Tidal Stream Turbine Operating Points

The operation of a tidal stream turbine can be adjusted depending on both the existing flow conditions that the turbine is exposed to and the desired performance output in relation to the idealised power output of the turbine. This can be achieved by adopting alternative strategies such as pitch or stall control.

A. Idealised power curve

The power and thrust of a tidal stream turbine are defined as

$$P = \frac{1}{2}\rho C_P A U_0^3 \tag{1}$$

and

$$F_x = \frac{1}{2}\rho C_T A U_0^2 \tag{2}$$

where ρ, A and U_0 are the water density, turbine swept area and inlet velocity, and C_P and C_T refer to the turbine's power and thrust coefficients, respectively. The variation of generated power with tidal stream flow speed is characterised by a power curve, as shown in Figure 1(a). Several regions of the operating curve can be considered: Region 1 refers to the velocity range above the cut-in speed U_{min} yet below the rated speed U_N, over which maximum power coefficient is sought such that the power generation increases cubically with the flow velocity. For flow speeds just below U_N in Region 2, the turbine starts to transition away from maximum C_P in order to be able to move towards constant power output. For flow speeds above the rated speed U_N, the turbine is operating in Region 3, generating rated power whilst C_P reduces with increasing speed. The power output is constant until the flow speed reaches the maximum value U_{max}. Above U_{max}, the turbine becomes vulnerable to overloading due to extreme forces, thus making turbine operation unsafe.

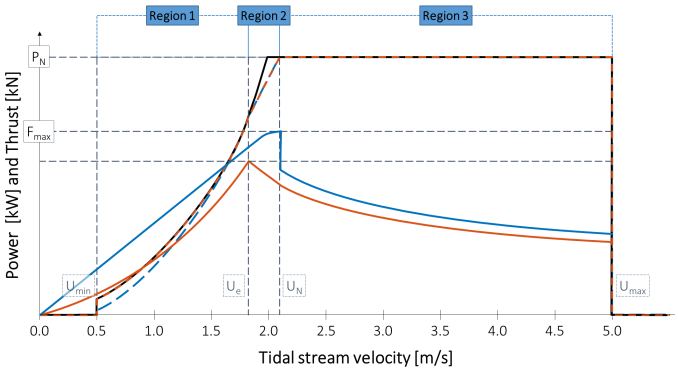

(a) Power (– –) and thrust (—) curves.

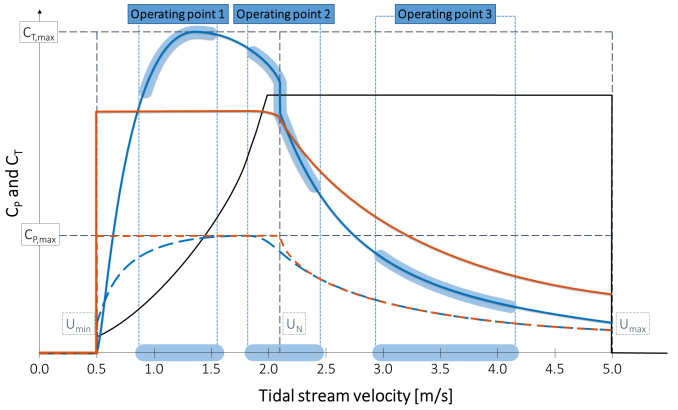

(b) C_P (– –) and C_T (—) curves.

Fig. 1. Qualitative representation of the variation of power and thrust (top) as well as C_P and C_T (bottom) of a tidal turbine with flow speed for fixed- (—) and variable-speed (—) control with respect to the idealised power curve (—). All curves are created using data from [13], [14]. The three chosen operating point ranges for the fixed-speed controlled turbine are also indicated in blue.

B. Control strategies

Control strategies are necessary to allow a turbine to operate as close to the ideal power curve (indicated in black in Figure 1(a)) as possible and maximise the efficiency of power generation. This includes both the maximum efficiency within the "partial-load regime" [15, p.2] in Region 1 as well as the full-load regime of Region 3 where the turbine operates at rated capacity and generates a constant power output. This can be achieved by applying a combination of pitch and speed control. The former control strategy operates on the principle that for high flow speeds the angle of attack α increases such that flow separation occurs above the leading edge of the blade which is referred to as 'stall' and results in a decrease of the mechanical torque and hence generated power [14], but also an undesirable increase in the thrust [16]. Thus, variable pitch control allows the operator to change the pitch angle and hence avoid stall for high flow speeds. The working principle of the latter is based on the turbine's ability to change its rotational speed depending on the flow velocity. Its particular impact on the performance of the turbine can be derived from the variation of both C_P and C_T with the tip-speed ratio (TSR) which is defined as the ratio of rotational rotor speed ω at the

blade tip and flow velocity such that

$$\lambda = \frac{\omega \cdot R}{U_0} \tag{3}$$

Hence, the variation of C_P and C_T with flow speed depends on the control strategy of the turbine. This is addressed in more detail in the subsequent section which presents the differences between a fixed-speed and a variable-speed turbine. It is assumed that both turbines are able to actively regulate pitch.

C. Fixed speed and variable speed turbines

For operation at fixed rotational speed, the TSR and consequently the variation of both C_P and C_T depend solely on the flow speed. Conversely, a variable speed turbine allows one to change the rotational speed and maintain the operation of the turbine at desirable operating points. The type of speed control has an impact on the variation of both power and thrust as well as each coefficient with flow speed. Applying pitch regulation, both speed control methods may be used to follow the ideal power curve comparatively closely, as sketched in Figure 1(a). The variable speed turbine allows the operator to change the rotational speed accordingly to the flow speed in order to maximise power generation when operating in Region 1. A fixed-speed control strategy, however, allows the power curve to intersect with the ideal power curve only at one point. This occurs when the flow speed coincides with the effective flow speed U_e and the turbine attains maximise efficiency. This point is also shown in Figure 1(b) where $C_P = C_{P,max}$ whilst the turbine with variable-speed control can operate at $C_{P,max}$ for the entire Region 1. Both turbine types then approach rated power between U_e and U_N and start operating at rated capacity when $U \geq U_N$ until the flow speed reaches U_{max}. Similarly, a turbine with variable-speed control is able to maintain a constant thrust coefficient in Region 1. Thus, the thrust acting on the turbine increases quadratically with flow speed, following equation 2. Beyond rated speed, both thrust and the value for C_T decrease as the turbine uses active pitch- and speed-control to maintain P_N. The fixed-speed control strategy, on the other hand, results in a almost linear increase of thrust below rated speed as the main focus lies on the maximisation of generated power. Hence, the maximum values of both the axial force and C_T for a fixed-speed controlled turbine exceed a variable-speed controlled turbine. Subsequently and beyond U_N, thrust and C_T decreases towards the upper limit of Region 2 and throughout Region 3 as the pitch of the turbine blades is controlled to maintain a constant power output at rated capacity [13]–[15].

D. Typical operating points

Following the presentation of the variation of thrust and power as well as their coefficients with flow speed and TSR, this section identifies several typical operating points for further investigation for in-array operation. Whilst the following observations can also be made for a turbine with variable-speed control, the authors refer subsequently to a fixed-speed controlled turbine only for the reason of simplicity. From the variation described in Figure 1 it becomes clear that there are three typical operating points for turbine thrust and power developed within the range of onset flow speeds experienced by a turbine in-array. Firstly, a turbine operating below rated speed where the power output is low but C_T high, secondly the region where the turbine operates close to rated speed where the power is maximum and C_T has decreased, and finally flow speeds above rated speed where the turbine operates at sustained peak power and a low value of C_T. These operating points are henceforth referred to as operating points 1, 2, and 3, and positioned in a C_T *v* U diagram as indicated in Figure 1(b). Finally, the previously defined C_T is also referred to as 'global' thrust coefficient and can be used to define the 'local' thrust coefficient c_x of an idealised actuator disc as a function of inlet velocity U_0 and disc velocity U_D such that

$$C_T = c_x \cdot \frac{U_D^2}{U_0^2} = c_x \cdot (1-a)^2 \tag{4}$$

III. Methods

Investigations of the impact of different turbine operating points on aggregated power output and thrust of an array were initially conducted with a CFD model. This analysis also informs the design of an experimental campaign with preliminary findings also reported. The CFD model employs a constant actuator disc (AD) model in a RANS solver whilst the experimental study employs porous discs to represent the stream-wise momentum extraction on a laboratory scale.

Both studies are presented and compared to results from an existing laboratory dataset of the wake and loading of tidal rotors [17] and a wake superposition model [11]. The existing experimental data is herein referred to as 'Experimental rotor study' and assessed the power and thrust per turbine and characteristics of the array wake for different array configurations at laboratory scale using horizontal axis three-bladed rotors. The superposition model defines each self-similar wake profile following [18]. With this approach, the effect of multiple turbines can be superimposed onto the downstream velocity profile using the derived equations for the centreline velocity deficit ΔU_{max} and wake half width $y_{1/2}$ such that

$$\frac{\Delta U_{max}}{U_0} = 0.864 \cdot (x/D)^{-\frac{1}{2}} - 0.126 \tag{5}$$

and

$$\frac{y_{1/2}}{R} = 0.412 \cdot (x/D)^{\frac{1}{2}} + 0.5 \tag{6}$$

which has shown good agreement with experimental studies [19]. Finally, to account for the increased bypass flow, a blockage correction following [11] is applied which is derived using a mass-conservation method.

A. Numerical study

The actuator disc (AD) model is implemented in the RANS CFD solver *STAR-CCM+* with a k-ω SST turbulence closure model. The AD model was chosen as it has been used in multiple studies before [21]–[23], represents a good compromise between computational costs and numerical accuracy, and

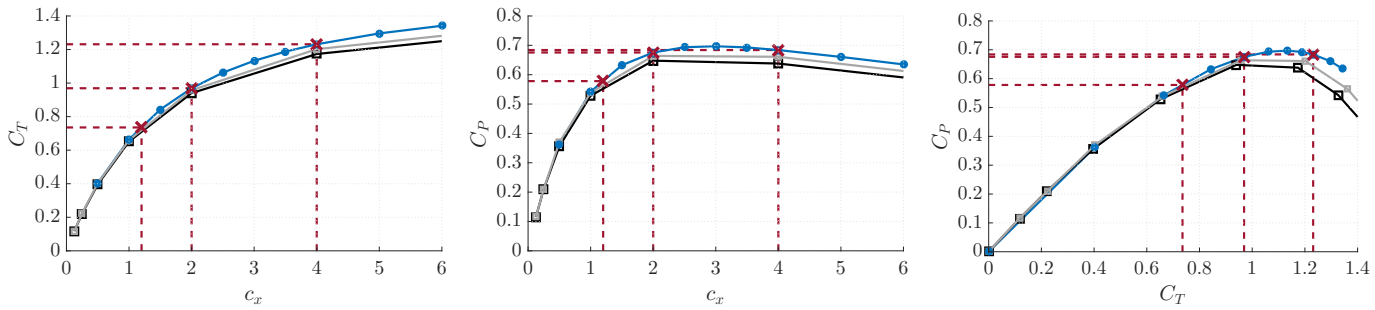

Fig. 2. RANS-AD single disc variation of global thrust coefficient C_T with local thrust coefficient c_x (left), effective power coefficient C_P with c_x (centre) and C_P with C_T (right). Results (–●–) with blockage 2.2% are compared to RANS-AD results from [20] for a single actuator disc with blockage of 4.8% (—) and 6.3% (—). The chosen typical operating points are indicated as ×.

allows a future comparison to the experimental study with porous discs. The simulation domain is set as a rectangular box with a length, width, and depth of 70D, 19D, and 1.68D, respectively, where D is the disc diameter. Applying Froude scaling to laboratory-scale dimensions, this configuration represents an 18 m diameter tidal stream turbine in a channel of 30 m depth. Values for the uniform free-stream velocity as well as k and ω are defined at the inlet boundary to represent the experiments. A slip condition is applied to the four plane stream-wise boundaries. Following the definition of the pressure drop across an AD where

$$\Delta p = \frac{1}{2}\rho C_T U_0^2 = \frac{1}{2}\rho c_x U_D^2 \tag{7}$$

the momentum sink term that defines the applied force per cell volume term and hence momentum extraction within the RANS-CFD solver is calculated using local parameters such that

$$\frac{F_x}{V} = \frac{\rho C_T U_0^2}{2 \cdot \Delta x} = \frac{\rho c_x U_{D,c}^2}{2 \cdot \Delta x} \tag{8}$$

where $U_{D,c}$ refers to the local cell-specific stream-wise velocity within the disc, whilst V and Δx are the cell volume and disc thickness, respectively. The force-per-volume term defined in above equation is defined such that it is calculated for each cell individually, meaning that the value for the disc velocity is taken as $U_{D,c}$ for each cell separately instead of averaging the stream-wise velocity across the entire disc domain.

This was firstly implemented in a single disc RANS-AD model to verify the respective variation of C_T and C_P with c_x following equation 4 and the definition of the effective power coefficient for an idealised actuator disc which can be inferred from the stream-wise force and U_D such that

$$C_P = \frac{F_x \cdot U_D}{\frac{1}{2}\rho A U_0^3} = C_T \cdot \frac{U_D}{U_0} = c_x \cdot (1-a)^3 \tag{9}$$

Note that this definition of C_P for porous discs aligned with partial fence theory [24] results in a higher value than the Betz limit. Using the results of Figure 2, Table I summarises the values of c_x with C_T and C_P for the three distinct operating points outlined previously in Section II.

TABLE I
OVERVIEW OF THE NUMERICAL CHARACTERISATION OF THE CHOSEN ROTOR OPERATING POINTS.

Operating point	1	2	3
Description	*Below rated power below rated speed*	*Rated power at rated speed*	*Sustained peak power above rated speed*
$C_{T,\text{Target}}$	1.25	0.89	0.64
c_x	4.0	2.0	1.2
$C_{T,\text{Actual}}$	1.25	0.96	0.74
C_P	0.68	0.68	0.58

The array layouts studied consist of up to 12 discs which are deployed across up to 3 rows. The transverse and longitudinal spacing is 1.5D and 4D, respectively. This includes the configurations in [17] and the reversed configuration to assess performance and loading of the same array layout during both phases of a bi-directional tidal flow. All array net performance coefficients reported are the sum of the individual turbine performance coefficients C_T and C_P. The different operating points are implemented through the variation of c_x across the array. Each array configuration regarding layout and operational strategy is referred to using following nomenclature: N row *x1 x2 x3 _ cx1 _ cx2 _ cx3* where N, x_i and $c_{x,i}$ refer to the number of rows in the array as well as number of turbines and operating point in form of the value of c_x in the i^{th} row, respectively.

For a 2row34_1.0_1.0 array, Figure 3 compares the RANS-AD model with results from both the experimental rotor study [17] and superposition [11] in terms of the mean C_T value per turbine and the transverse profile of the stream-wise velocity deficit. Regarding the former, the presented values show the mean value of C_T for each turbine as a fraction of the mean C_T value of a single disc in isolation. These values are 0.97 and 0.84 for the present RANS-AD model and experimental rotor study, respectively. Figure 3 shows reasonable agreement for the rotor loading between RANS-AD and experimental results. Whilst the front row is not experiencing the same increase, the RANS-AD still captures the higher thrust due to the increased blockage compared to a single rotor. Regarding the downstream row, RANS-AD is able to capture the trend

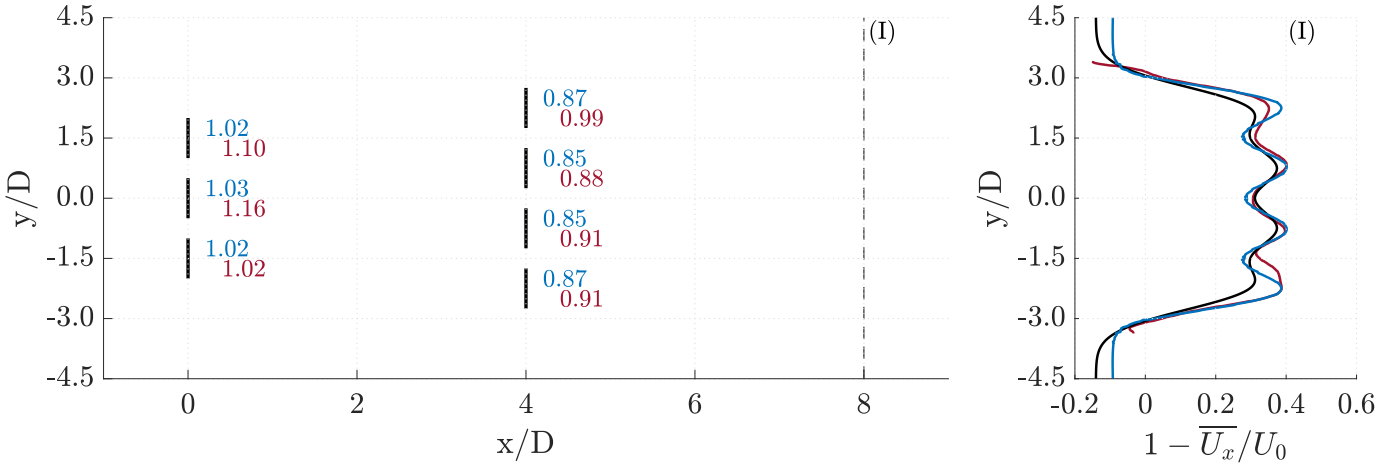

Fig. 3. Mean values of thrust coefficient as fraction of single device $C_{T,\text{single}} = 0.97$ from RANS-AD (blue text) and $C_{T,\text{single}} = 0.84$ from published experimental data (red text) [17]. Transverse profile of velocity deficit also shown at (I) 4D downstream of the 2nd row from RANS-AD (—), published experimental data (—), and superposition (—).

of increased loading for the outer rotors but underpredicts the variation of the loading along the row slightly. The disagreement could be caused by the change of rotational speed in the experimental rotor study due to the fact that the applied torque was defined as constant which results in a change of both the operating point and C_T for each rotor. Additionally, the AD model neglects rotor and wake rotation which results in a lower rate of mixing between individual wakes than observed in the experiments. The downstream velocity deficit variation shows good agreement between all three examined studies. This is indicated by the average velocity deficit across the span-wise width of a row where $y/D \leq \pm 2.75$. The mean value for RANS-AD is 0.325 m/s which is within 5% of both the mean values for the superposition model and the experimental rotor study, respectively.

B. Experimental study

The experiments were carried out in the large flume of the State Key Laboratoy of Hydro-science and Engineering at Tsinghua University in Beijing, China. The flume has a working section of approx. 25 m length and 2.1 m width. The inflow and outflow regions are slightly wider at 3.5 m width. Hence, the experimental setup was positioned at a sufficient distance downstream to avoid any impact of the transition to the narrower cross-section. The water depth is regulated by controlling the sluice gate opening at the end of the flume. In order to achieve a water depth of 0.185 m and produce similar conditions in terms of Froude number (Fr = 0.19), depth-to-diameter ratio ($d/D = 1.67$ where D = 0.11 m) and global blockage ($\varepsilon = 5A_D/Wd = 12.5\%$) as in the experimental rotor study [17], the sluice gate opening was set to a mean value of 22.5 mm. The discs were manufactured from 4 mm thick PVC material and laser cut holes were distributed uniformly across the discs cross-section using three concentric rings similarly to [25].

Due to the complexity of the relationship between C_T and the geometrical porosity ϕ of a porous disc [26], previous measurements [20] are used as guideline for the design of the porous discs in form of the number of holes required N_H in relation to disc and hole diameters D and d_H where

$$\phi = \frac{A_{Open}}{A_{Solid}} = \frac{N_H \cdot d_H^2}{D - N_H \cdot d_H^2} \tag{10}$$

TABLE II
OVERVIEW OF THE EXPERIMENTAL CHARACTERISATION OF THE CHOSEN ROTOR OPERATING POINTS USING POROUS DISCS.

Operating point	1	2	3
Description	*Below rated power below rated speed*	*Rated power at rated speed*	*Sustained peak power above rated speed*
$C_{T,\text{Target}}$	1.25	0.89	0.64
ϕ	0.3	1.0	1.4
N_h	15	31	36

Table II summarises target values for C_T and corresponding porosity and number of holes required. Similarly to the numerical study, the experimental setup included multiple disc configurations in various array layouts of up to 3 rows and 12 discs with at least 3 discs in each row. Each disc was mounted at its axis to a horizontal rod downstream of a vertical support tower of diameter 0.09D. Each tower was affixed via a pivot onto a horizontal gantry spanning across the width of the flume. The rotational movement of the support tower and disc around a pivot point could be controlled manually. Measurements were taken of both the downstream velocities and the stream-wise force on each disc within all array configurations (Figure 4). Each disc loading was measured using the ZhiQu Push-Pull Digital Force Gauge DS2-10N. The pressure gauge has a force range of ±10 N and can measure with an accuracy of up to ±0.2%. Force measurements were taken at a sample rate of 5.33 Hz and with a sampling time of 10 minutes. The force gauge was fixed onto a horizontal metal plate and fitted with an extended v-shaped tip to ensure an acceptable contact point between force gauge and tower. Time-varying velocities

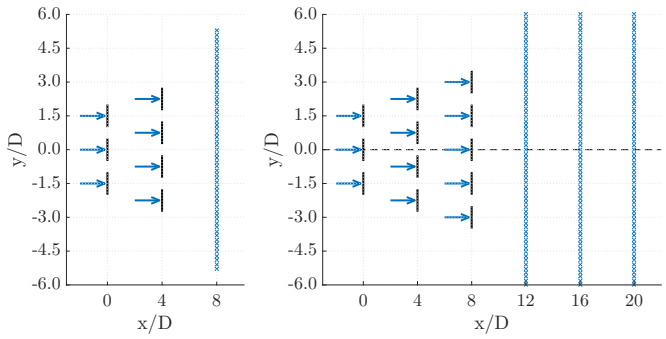

Fig. 4. Exemplary graphical overview of experimental measurements for 2row34 (left) and 3row345 (right) array layouts. Thrust measurements (→) are taken on each disc individually. Interval for wake measurements (×) across transverse profile is 2 cm between each point.

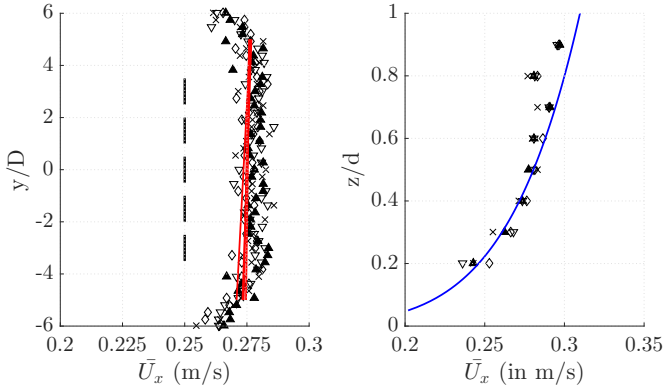

(a) Transverse profile. (b) Depth profile.

Fig. 5. 1-minute averaged measurements of ambient stream-wise velocity for locations along transverse (a) and depth at mid-span (b) at 0D (▲), 4D (▽), 8D (×), and 16D (◊). Least-squares linear fits (—) and 1/7$^{\text{th}}$ power law (—). Width span of row of 5 discs as reference added as solid black lines (—) to the transverse velocity profile plot.

were measured at mid-depth with a sample rate of 200 Hz using a NORTEK Vectrino+ Acoustic Doppler Velocitymeter (ADV). The sampling period of each measurement was 60 seconds unless specified otherwise to minimise uncertainty of measurements. The Vectrino+ ADV was operated with a velocity range of ±1 m/s, a sample dimension of 3 mm and transmit length of 8.7 mm (Nortek 2015) and was mounted on a gantry with an automated traverse.

Figure 5 shows the variation of the stream-wise velocity of the ambient flow in both transverse direction and across the vertical flow plane. The mean ambient flow velocity within the applicable width of the working section is 0.278 m/s. Within the cross-sectional width of a row of 5 discs (y = ± 3.5D), the RMSE of the mean flow velocity for various downstream locations ranges between ±3%. There was nearly linear variation of stream-wise velocity across this width, but this was small at less than 1.7% of the mean flow speed. Turbulence intensity is measured to be around 9.0%.

In Figure 6, the experimental results for both turbine loading and downstream velocity deficit of the 2row34_1.0_1.0 array are compared to the same published datasets as in the section above. Similarly to Figure 3, the mean values of C_T are shown as a fraction of the single rotor C_T which is 0.78 for this experimental study. The experiments capture a marginal increase in thrust in the front row associated with local blockage effects. However, as with the RANS-AD, the increase is not as significant as in the experimental rotor study. Regarding the downstream disc loading, both experimental studies show good agreement with the exception of the disc at y = +0.75D for which higher thrust is reported. This asymmetry is being investigated. Whilst the experiments agree well with the maximum velocity deficit downstream of the centre of each disc, they overpredict the bypass flow between the discs at 4D downstream. This can in part be attributed to the lower turbulence intensity of the experiments

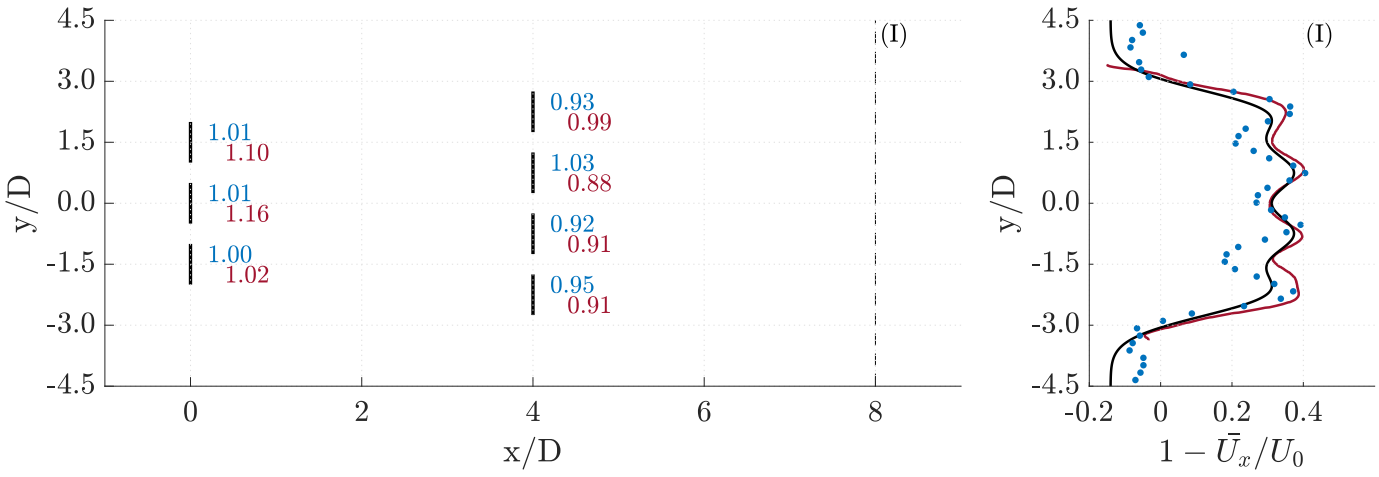

Fig. 6. Mean values of thrust coefficient as fraction of single device $C_{T,\text{single}} = 0.78$ from experiments at Tsinghua University (blue text) and $C_{T,\text{single}} = 0.84$ from published experimental data (red text) [17]. Transverse profile of velocity deficit also shown at (I) 4D downstream of the 2$^{\text{nd}}$ row from experiments at Tsinghua University (•), published experimental data (—), and superposition (—).

of 9% compared to the experimental rotor study which reduces the overall wake mixing and therefore results in a more persistent wake shape. In addition, the porous discs used in the experiments do not incur any rotational movement within the downstream wake and a higher instantaneous inter-array blockage which results in a slower turbulent mixing and higher shear profile, respectively. This underprediction can be seen in particular when comparing the average velocity deficit across $y/D \leq \pm 2.75$. The value of 0.29 m/s represents a reduced value of 19% and 8% compared to the superposition model and the experimental rotor study, respectively.

IV. Results

The three previously defined operating points are used to characterise the effect on the net array thrust in both the numerical and experimental setup in form of the net array thrust coefficient $C_{T,net}$. As previously mentioned, the net array values of C_T and C_P are calculated as the sum of all individual turbine coefficients. Following the comparison of the results from both the numerical and experimental studies with previously published data where $c_x = 2.0$ and $\phi = 1.0$, the same operating strategies are used as baseline for an array with 12 turbines deployed across 3 rows. In order to assess the impact of bi-directional flow, the subsequent section shows results for both a 3row345 and 3row543 array.

For the numerical study, Figure 7 shows the values of C_T and C_P for each individual turbine and the aggregated coefficients $C_{P,net}$ and $C_{T,net}$ as a whole in bi-directional flow operating at $c_x = 2.0$. Both net array coefficients increase by 4.5% and 7.5% from 9.83 to 10.27 and 6.36 to 6.84, respectively, when changing from a 3row345 to a 3row543 array layout. This is in particular due to the increased individual performance coefficients in the upstream row which is caused by the higher blockage ratio across the front row. Additionally, there is less wake mixing within the central region of the array due to the smoother transition between the low and high velocity fields in the wake and bypass areas, respectively, and hence a less defined shear profile. In combination with the accelerated inter-array bypass flow, as indicated in Figure 8, this has a positive effect on the performance of the two central turbines in the middle row. Lastly, the performance of the downstream row turbines within both array configurations is very similar with the exception of the two outermost turbines in the 3row345 array which take advantage of the outer-array bypass flow acceleration and perform almost as well as the upstream row turbines.

In comparison to the baseline operating strategy, the net array performance coefficients decrease and increase for an operating strategy where $c_x = 1.2$ and $c_x = 4.0$, respectively. An overview of the absolute net array values as well as the relative change is summarised in Table III. For the former op-

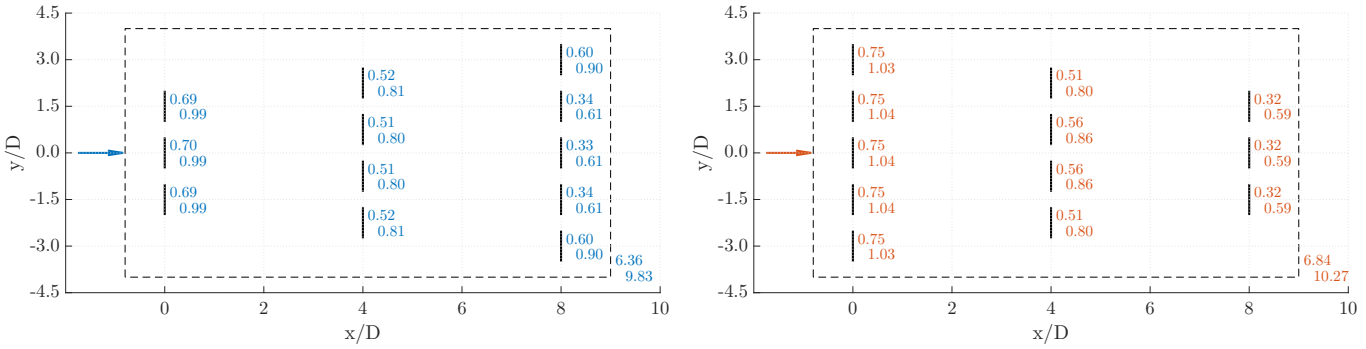

Fig. 7. Individual turbine and net array $C_{P,i}$ (top) and C_T (bottom) values for a tidal array with 12 turbines across three rows in bi-directional flow. Each turbine is operating at $c_x = 2.0$. The turbine values are presented next to each turbine while the array values are shown in the bottom right and left corner. The arrows indicate the direction of flow.

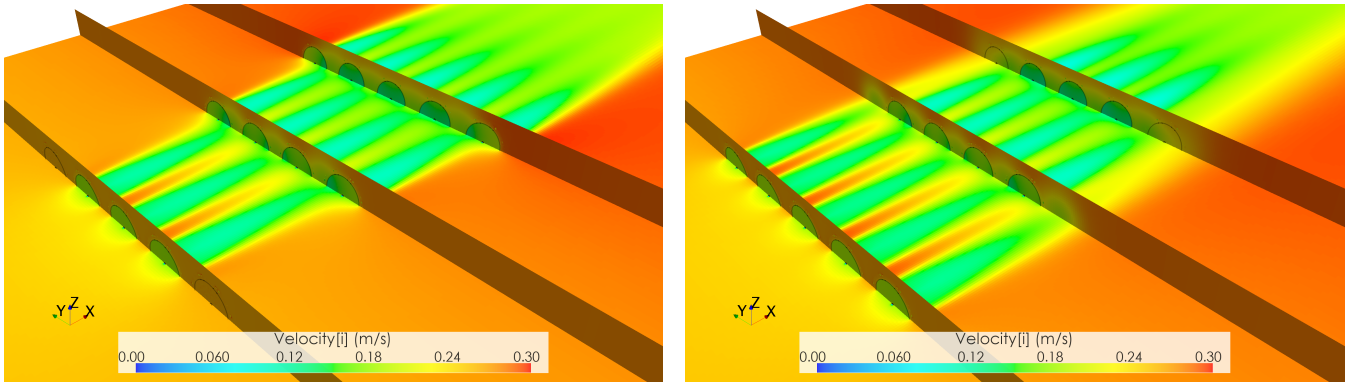

Fig. 8. Qualitative contour plots for a tidal stream turbine array with 12 turbines across three rows in bi-directional flow corresponding to Figure 7. Each turbine is operating at $c_x = 2.0$.

TABLE III

SUMMARY AND COMPARISON OF THE PERFORMANCE COEFFICIENTS FOR EACH OPERATING STRATEGY AND FLOW DIRECTION. ALL VARIABLES AND VALUES WITH SUBSCRIPT *net* ARE REFERRING TO THE NET ARRAY VALUES.

Study	Configuration		$C_{T,net}$	$\Delta C_{T,net}$	$C_{P,net}$	$\Delta C_{P,net}$	$\max \Delta C_T$	$\max \Delta C_P$	$C_{T,net}/C_{P,net}$
RANS-AD	$c_x = 2.0$	$\rightarrow$ 3-4-5	9.83	**N/A**	6.36	N/A	39%	52%	1.55
		$\rightarrow$ 5-4-3	10.28	**+4.8%**	6.84	+7.5%	43%	57%	1.50
	$c_x = 1.2$	$\rightarrow$ 3-4-5	7.87	**-20.0%**	5.85	-7.9%	30%	41%	1.35
		$\rightarrow$ 5-4-3	8.08	**-21.3%**	6.11	-10.6%	23%	45%	1.32
	$c_x = 4.0$	$\rightarrow$ 3-4-5	12.04	**+22.4%**	6.12	-3.7%	47%	61%	1.97
		$\rightarrow$ 5-4-3	12.77	**+24.2%**	6.79	-0.7%	54%	69%	1.88
Experiments	$c'_x = 1.32$	$\rightarrow$ 3-4-5	8.82	**N/A**	–	–	35%	–	–
		$\rightarrow$ 5-4-3	8.98	**+1.8%**	–	–	33%	–	–
	$c'_x = 0.93$	$\rightarrow$ 3-4-5	7.02	**-20.4%**	–	–	39%	–	–
		$\rightarrow$ 5-4-3	7.16	**-18.8%**	–	–	31%	–	–
	$c'_x = 4.44$	$\rightarrow$ 3-4-5	14.37	**+62.9%**	–	–	35%	–	–
		$\rightarrow$ 5-4-3	15.36	**+74.1%**	–	–	54%	–	–

erating strategy, net thrust decreases by approx. 20% for both flow directions whilst the power is reduced by 8% and 10.5% for the 3row345 and 3row543 configurations, respectively. The comparatively high reduction in thrust is caused by the lower imposed thrust coefficient which, in turn, maintains a higher energy flux across the array and hence does not reduce the inferred power as significantly. This more steadily distributed extraction of momentum from the flow also leads to a smaller range between highest and lowest loading experienced by the turbines compared to the other two operating strategies. On the other hand, the thrust increases by more than 20% for both flow directions if the operating strategy is changed to the higher c_x value. However, this increase in thrust does not have a positive impact on the inferred power as it decreases by approx. 1-4% depending on the flow direction.

Similar trends can be observed for the experimental study with net array values summarised in Table III where the given values for c'_x refer to the equivalent porosities used within the experimental study. However, the values for c_x and c'_x are not identical and so a direct comparison between the CFD model and disc experiments is not given at this stage. The same behaviour is observed for reversing flow with baseline c_x and c'_x values of 2.0 and 1.32, respectively, where the net thrust increases for the 5-4-3 array layout. Additionally, a similar percentage change of ΔC_T is observed for a 30% reduction of the experimental c'_x compared to a 40% reduction of the numerical c_x. For a c'_x value increased by a factor of 3.3 compared to the baseline of $c'_x = 1.32$, the change of $\Delta C_{T,net}$ is in the same direction but significantly greater magnitude than for increasing c_x. Due to the measurement of thrust only during the experiments, no values for the power coefficient are given here.

Lastly, we consider the thrust-to-power ratio defined as the fraction of $C_{T,net}$ over $C_{P,net}$ to assess the overall array performance from RANS-AD. Following the 'basin efficiency' definition in [24], this ratio quantifies the units of thrust that are imposed on the flow in order to produce a single unit of power. As shown in Table III, this ratio improves for lower values of c_x and differs for each array with flow direction. However, it should be recognised that these values may be higher for an array of turbines which can only develop lower C_P values than the idealised actuator disc approach used here.

V. IMPLICATIONS

The previous section showed agreement between the trends of a numerical RANS-AD and an experimental study using porous discs. The implications of an adaptive operating strategy on the performance and loading of an array through a tidal cycle are briefly explored using an idealised model of head-driven channel flow. The model is defined in [27] and applied in a similar manner to [12]. However, a change derived from the definition of the basin efficiency [24] was implemented to account for the impact of the power removed rather than the power extracted on the mean channel velocity U_c where

$$\eta = \frac{Power\ extracted}{Power\ removed} = \frac{P_{ext}}{F_x \cdot U_c} \tag{11}$$

and thus

$$F_x = \frac{P_{ext}}{U_c} = C_1 \cdot \left(U_0^2 - U_c^2\right) \tag{12}$$

Here, C_1 is a constant describing the channel characteristics. The 12 turbine array layout employed in the RANS-AD study is considered to allow assessment of the array performance through a bi-directional tidal cycle. Each turbine has a diameter of 16 m, a rated speed of 2.25 m/s and a rated power of 1 MW, resulting in a rated array power of 12 MW. The channel has a length, width, and depth of 1 km, 300 m, and 27 m, respectively. These values ensure that the same blockage ratio is applied as in both the array-scale RANS model and experimental study. The values presented in Table III for the numerical study are then used to calculate the array power output and net thrust for two different scenarios; firstly, the operating point is kept constant across the entire

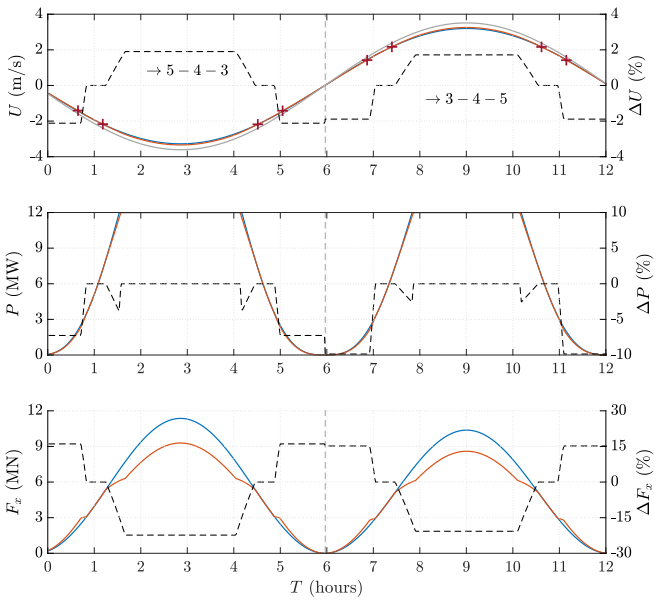

Fig. 9. Initial (—) and channel velocity, array layout and change of operating point (+) (top) as well as net power output (centre) and net thrust (bottom) for a constant (—) and adaptive (—) operating strategy including the change relative to the constant operating strategy (—) with corresponding axis on the right over a tidal cycle with a time period of approx. 12 hours.

flow speed range such that the net array values of $C_{T,net}$ and $C_{P,net}$ are taken from $c_x = 2.0$, only. Secondly, an adaptive operating strategy is applied such that the aforementioned array performance coefficients are taken from different c_x values depending on the flow speed as follows:

- $U_c \leq 1.50$ m/s: $c_x = 4.0$
- 1.70 m/s $< U_c \leq 2.25$ m/s: $c_x = 2.0$
- $U_c > 2.75$ m/s: $c_x = 1.2$

Here, each of the three operating points modelled are applied to discrete velocity ranges whilst $C_{P,net}$ and $C_{T,net}$ are interpolated for velocity values outside the given range to provide a smooth transition between these discrete operating points.

Figure 9 shows the variation of flow speed in the idealised channel as well as the power output and net thrust for the described array for both operating strategies over a time duration of 12 hours. The undisturbed tidal current changes direction approximately after 6 hours so that the tidal array is exposed to a tidal current from both directions for equal time intervals. The variation and maximum flow speed for the given time period, however, is not equal for both flow directions. Whilst the average and maximum flow speed in the first six hours are 2.39 m/s and 3.61 m/s, both reduce by 6.2% and 2.7% for the second time period, respectively.

For the constant operating point strategy, it can be seen that the existence of the array reduces the mean channel velocity by approx. 9.1%. The array reaches its rated power capacity of 12 MW just after the flow speed exceeds 2.5 m/s. The mean power output over the given 12 hour time span is 7.1 MW which results in a net energy yield of 85.2 MWh for the same time span. 52.1% and 47.9% of the given yield are produced by the 5-4-3 and 3-4-5 array layout, respectively. This can be attributed to the asymmetrical nature of the bi-directional flow. Whilst power is capped at 12 MW, the thrust increases steadily until it reaches its maximum at maximum flow speed. Due to the comparatively lower value of $C_{T,net}$ as well as the uneven bi-directional flow distribution over the assessed time period, the maximum thrust applied by the 3-4-5 array layout of 10.4 MN is 8.7% lower than the 5-4-3 layout. This is also observed for the average net thrust which reduces by 12.3% from 5.9 MN to 5.2 MN.

For the adapted operating strategy approach, it is apparent that such an approach can be beneficial with regards to the variation of applied net thrust. For low flow speeds the array imposes a comparatively higher thrust because $C_{T,net}$ is higher for $c_x = 4.0$ than $c_x = 2.0$ as outlined previously in Table III. In contrast, the imposed thrust decreases significantly in the high flow speed regime. The relative change to the constant operating point strategy is shown in Figure 9 by the dashed black line. Here, the average and maximum thrust decreases by 12.9% and 11.7% as well as 18.3% and 17.2% for the 5-4-3 and 3-4-5 array layouts, respectively. The impact of the changed model formulation can be seen in the change of the channel velocity. Whilst the comparatively higher imposed thrust at low flow speeds results in the array with the adapted operating strategy experiencing a 2% lower flow speed, the lower imposed thrust at high flow speeds leads to a less significant change of the channel velocity. Hence, the array produces 84.7 MWh over the 12 hour period which equates to 0.6% less power compared to the constant operating strategy. Thus, the array performance experiences an almost negligible negative impact despite the outlined reduction of thrust. Finally, due to the relatively low blockage of less than 10%, the change of the channel velocity is not as significant as the thrust reduction might suggest. Nonetheless, in this scenario the latter is likely to be preferable in terms of the reduced modification of the undisturbed flow.

VI. Conclusion

This paper presents a numerical and experimental investigation of the effect of changing operating points on the net thrust and power of a tidal stream turbine array. Three operating points are considered to represent regions of the power curve of a fixed-speed controlled tidal turbine using characteristic thrust coefficient values below rated speed, near rated speed, and above rated speed, and subsequently translated to an equivalent value for local thrust coefficient c_x and porosity ϕ. These parameters are subsequently used to define the momentum extraction in a numerical RANS-AD and an experimental study with porous discs, conducted at Tsinghua University in Beijing, respectively. The experiments show good consistency and accuracy with regards to characterising the ambient flow as well as turbine loading and wake measurements. For both studies, net thrust, and in case of the RANS-AD, power output are determined in form of aggregated thrust and power coefficients for the array.

Both studies are assessed separately relative to prior experiments for similar array configurations of up to 12 turbines deployed across 3 rows in a 3-4-5 array layout. The same array layouts subject to reversed flow are also considered. Each study produces results for the individual turbine loading as well as downstream transverse velocity variation and the wake structures measured are similar to those of prior experiments and a wake superposition model. This is in particular demonstrated by the accuracy of the predicted average velocity deficit which is not greater than approx. 5% and 19% for both studies, respectively.

The RANS AD CFD and porous disc experiment exhibit similar trends in terms of variation of $C_{T,net}$ with local thrust coefficient (c_x) and disc porosity (ϕ). Higher c_x values result in higher values of aggregate thrust and the reversed flow case of a 5-4-3 array develops higher thrust than the 3-4-5 layout for all values of c_x. The results for $C_{T,net}$ from the numerical RANS-AD model are used to characterise the effect of different operating strategies on the net power output, thrust and environmental footprint of the array on the resource using a channel-scale model. It shows that an adaptive operating strategy with a changing array operating point is able to reduce the average thrust imposed on the resource over a time span of 12 hours by 12.3% whilst the energy yield over the same time span is decreased by a comparatively insignificant 0.6%.

Thus, it is shown that an adaptive operating strategy can provide an improvement on the environmental impact whilst still generating a similar energy yield. This can have valuable implications with regards to both modelling and assessing the power output from large-scale tidal farms as well as the operational flexibility of the latter to provide future support for electrical grids. Future work includes the adjustment and re-evaluation of the RANS-AD model for local thrust coefficient values as measured in the experimental study and the potential implementation of the latter in a more sophisticated channel-scale shallow water model.

ACKNOWLEDGEMENTS

The first author acknowledges financial support from EPSRC (EP/L016141/1) through the Power Networks Centre for Doctoral Training. The authors of this paper also received funding from the EU-China IRES-8 Mobility Project under EU Contract Number No ICI+/2014/347-910. The contents reflect only the authors view and the European Union is not liable for any use that may be made of the information contained therein.

REFERENCES

[1] The Carbon Trust, Black & Veatch, and N.power, "UK tidal current resource & economics," London, UK, Tech. Rep., 2011.

[2] Department for Business and Energy & Industrial Strategy, "Energy Consumption in the UK," Department for Business, Energy & Industrial Strategy, London, UK, Tech. Rep., 2016.

[3] Atlantis Resources, "MeyGen Phase 1A completes construction phase and officially enters 25 year operations phase," *MeyGen News*, 2018.

[4] National Grid, "Future Energy Scenarios," Warwick, UK, Tech. Rep., 2015.

[5] ——, "System Operability Framework 2015," National Grid Electricity Transmission plc., Warwick, UK, Tech. Rep. November, 2015.

[6] R. Vennell, "The energetics of large tidal turbine arrays," *Renewable Energy*, vol. 48, pp. 210–219, dec 2012.

[7] T. A. A. Adcock, S. Draper, G. T. Houlsby, A. G. L. Borthwick, and S. Serhadlioglu, "The available power from tidal stream turbines in the Pentland Firth," *Proc. of the Royal Society A: Mathematical, Physical and Engineering Sciences*, vol. 469, no. 2157, pp. 20 130 072–20 130 072, 2013.

[8] R. Vennell, S. W. Funke, S. Draper, C. Stevens, and T. Divett, "Designing large arrays of tidal turbines: A synthesis and review," *Renewable and Sustainable Energy Reviews*, vol. 41, pp. 454–472, jan 2015.

[9] R. Vennell, "Tuning turbines in a tidal channel," *Journal of Fluid Mechanics*, vol. 663, pp. 253–267, nov 2010.

[10] S. Funke, P. Farrell, and M. Piggott, "Tidal turbine array optimisation using the adjoint approach," *Renewable Energy*, vol. 63, pp. 658–673, 2014.

[11] P. Stansby and T. Stallard, "Fast optimisation of tidal stream turbine positions for power generation in small arrays with low blockage based on superposition of self-similar far-wake velocity deficit profiles," *Renewable Energy*, vol. 92, pp. 366–375, 2016.

[12] C. Hachmann, T. Stallard, and P. Stansby, "Simulation of groups of tidal rotors with support structures," in *Proc. of the 12th European Wave and Tidal Energy Conference*, Cork, Ireland, 2017, pp. 1–9.

[13] T. Burton, N. Jenkins, D. Sharpe, and E. Bossanyi, *Wind Energy Handbook*, 2nd ed. Chichester, UK: John Wiley & Sons, Ltd, 2011.

[14] B. Whitby and C. E. Ugalde-Loo, "Performance of pitch and stall regulated tidal stream turbines," *IEEE Transactions on Sustainable Energy*, vol. 5, no. 1, pp. 64–72, 2014.

[15] E. J. Novaes Menezes, A. M. Araújo, and N. S. B. da Silva, "A review on wind turbine control and its associated methods," *Journal of Cleaner Production*, vol. 174, pp. 945–953, 2017.

[16] F. D. Bianchi, R. J. Mantz, and H. De Battista, *Wind Turbine Control Systems*, ser. Advances in Industrial Control. London: Springer London, 2007.

[17] A. Olczak, T. Stallard, T. Feng, and P. K. Stansby, "Comparison of a RANS blade element model for tidal turbine arrays with laboratory scale measurements of wake velocity and rotor thrust," *Journal of Fluids and Structures*, vol. 64, pp. 87–106, 2016.

[18] T. Stallard, T. Feng, and P. K. Stansby, "Experimental study of the mean wake of a tidal stream rotor in a shallow turbulent flow," *Journal of Fluids and Structures*, vol. 54, pp. 235–246, 2015.

[19] D. Lande-Sudall, T. Stallard, and P. Stansby, "Experimental Study of the Wakes due to Tidal Rotors and a Shared Cylindrical Support," in *Proc. of the 12th European Wave and Tidal Energy Conference*, Cork, Ireland, 2017, pp. 1–10.

[20] T. Stallard, R. Willden, S. McIntosh, and T. Feng, "Design and specification of ducted disc experiments," Energy Technology Institute (ETI), Loughborough, UK, Tech. Rep., 2012.

[21] S. Gant and T. Stallard, "Modelling a tidal turbine in unsteady flow," *Proc. of the 18th International Offshore and Polar Engineering Conference 2008*, vol. 8, pp. 473–480, 2008.

[22] M. E. Harrison, W. M. J. Batten, and A. S. Bahaj, "A blade element actuator disc approach applied to tidal stream turbines," in *OCEANS 2010 MTS/IEEE SEATTLE*, 2010, pp. 1–8.

[23] W. M. J. Batten, M. E. Harrison, and A. S. Bahaj, "Accuracy of the actuator disc-RANS approach for predicting the performance and wake of tidal turbines," *Philosophical Transactions of the Royal Society A: Mathematical, Physical and Engineering Sciences*, vol. 371, no. 1985, pp. 20 120 293–20 120 293, jan 2013.

[24] T. Nishino and R. H. J. Willden, "The efficiency of an array of tidal turbines partially blocking a wide channel," *Journal of Fluid Mechanics*, vol. 708, pp. 596–606, 2012.

[25] S. Draper, T. Stallard, P. Stansby, S. Way, and T. A. A. Adcock, "Laboratory scale experiments and preliminary modelling to investigate basin scale tidal stream energy extraction," in *Proc. of the 10th European Wave and Tidal Energy Conference*, no. Proc. of the 10th European Wave and Tidal Energy Conf., Aalborg, Denmark, 2013.

[26] S. C. Cooke, R. H. J. Willden, B. W. Byrne, T. Stallard, and A. Olczak, "Experimental Investigation of Thrust and Power on a Partial Fence Array of Tidal Turbines," in *Proc. of the 11th European Wave and Tidal Energy Conference*, no. 1920, Nantes, France, 2015, pp. 1–10.

[27] I. G. Bryden and S. J. Couch, "How much energy can be extracted from moving water with a free surface: A question of importance in the field of tidal current energy?" *Renewable Energy*, vol. 32, no. 11, pp. 1961–1966, 2007.